Microstructural Analyses of ATI 718Plus® Produced by Wire-ARC Additive Manufacturing Process

G. ASALA, A.K. KHAN, J. ANDERSSON, and O.A. OJO

A detailed microstructural study of ATI 718Plus superalloy produced by the wire-arc additive manufacturing (WAAM) process was performed through the use of scanning electron microscopy (SEM), transmission electron microscopy (TEM), electron probe micro-analysis (EPMA), and electron backscatter diffraction (EBSD). Extensive formation of eutectic solidification microconstituents including Laves and MC-type carbide phases, induced by micro-segregation, are observed in the build of the alloy in the as-deposited condition. Notwithstanding the significant segregation of niobium (Nb), which has been reported to promote the formation of the δ-phase in ATI 718Plus, only η-phase particles are observed in the deposit. Excessive precipitation of η-phase particles is found to be linked to Laves phase particles that are partially dissolved in the deposit after post-deposition heat treatment (PDHT). The EBSD analysis shows a high textured build in the $\langle 100 \rangle$ directions with only a few misoriented grains at the substrate–deposit boundary and the top of the deposit. Investigation on the hardness of the build of the alloy, in the as-deposited condition, showed a softened zone about 2 mm wide at the deposited metal heat affected zone (DMHAZ), which has not been previously reported and potentially damaging to the mechanical properties. An extensive analysis with the use of both microstructural characterization tools and theoretical calculations shows that the DMHAZ has the lowest volume fraction of strengthening precipitates (γ' and γ'') in terms of their number density, which therefore induces the observed softness. Delayed re-precipitation kinetics and the extent of the precipitation of γ' and γ'' in the DMHAZ which is related to the diffusion of segregated solute elements from the interdendritic regions are attributed to this phenomenon. The microstructural analyses discussed in this work are vital to adequate understanding of properties of ATI 718Plus produced by the additive manufacturing process technique.

DOI: 10.1007/s11661-017-4162-2

I. INTRODUCTION

ATI 718Plus (718Plus) is a nickel (Ni)-based superalloy developed by Allegheny Technologies Incorporated (ATI), and designed to replace its baseline alloy, IN 718, in aero-engines and power plants.[1–3] The alloy is reported to show improved thermal stability of approximately 328 K (55 °C) above that normally stipulated for IN 718 while maintaining the formability and weldability of IN 718.[4–9] The improved stability in 718Plus is achieved through changes to the composition of IN 718 in which iron (Fe) is partially replaced by cobalt (Co) and tungsten (W), while the content and ratio of aluminum (Al) and titanium (Ti) are modified.[4,10–12] This allows for the replacement of metastable γ'' ($D0_{22}$ body-centered-tetragonal (BCT)) precipitates in IN 718 with more stable γ' ($L1_2$ face-centered-cubic (FCC)) precipitates as the main strengthening phase in 718Plus which has also been found to accelerate its strengthening kinetics.[9,13] Furthermore, the increase in Al in 718Plus has been attributed to the formation of η ($D0_{24}$ hexagonal) phase particles at the grain boundaries, versus the orthorhombic δ phase (D0a, Ni_3Nb particles in IN 718.[14,15]

To facilitate the application of 718Plus, many traditional manufacturing processes used in producing IN 718 components have been investigated with relative success.[5,16–18] However, few studies have been carried out on additive manufacturing (AM) of 718Plus. In the pioneering work of Idell *et al.*[19,20] on the as-deposited microstructure of laser-sintered 718Plus. After carrying out an X-ray diffraction analysis, they suggested that γ' precipitates are present in the γ matrix of the deposit. Surprisingly, no η phase particles were reported, and

G. ASALA is with the Department of Mechanical Engineering, University of Manitoba, Winnipeg, R3T 5V6, Canada. A.K. KHAN and O.A. OJO are with the Department of Mechanical Engineering, University of Manitoba and also with the Manitoba Institute for Materials, University of Manitoba, Winnipeg, R3T 2N2, Canada. Contact e-mail: olanrewaju.ojo@umanitoba.ca J. ANDERSSON is with the Department of Engineering Science, University West, 461 86, Trollhättan, Sweden.

Manuscript submitted February 4, 2017.
Article published online June 13, 2017

their absence was attributed to the abnormal increase in niobium (Nb) concentration at the interdendritic regions thus promoting the formation of the orthorhombic δ phase instead. In addition, the presence of Laves phase particles, which is induced by the micro-segregation of Nb and commonly observed in additive manufactured IN 718[21,22] and reported in the fusion zone of welded 718Plus,[7,23] was not reported in the study. It is, however, known that some of these microconstituents, which form during the solidification stage of the process, can be extremely small in size and, thus, could be very challenging to identify through the use of conventional microscopy and spectroscopy techniques. The use of advanced analytical techniques like the TEM often becomes imperative. In order to successfully apply AM to manufacture 718Plus components, there is the need to increase the understanding of the microstructural changes and obtain in-depth knowledge of the microstructural characteristics of the deposit. This increase in knowledge is essential for building trust in the application of this material especially in the aerospace industries and also in developing material models which will help to optimize and tailor the material properties for intended applications. Therefore, the objective of this research was to perform detailed analyses of the microstructures developed during WAAM of 718Plus, including by the use of TEM, which would provide valuable knowledge crucial to understanding the properties of the material produced by additive manufacturing process.

II. EXPERIMENT AND METHOD

A. *Deposition by Using WAAM*

718Plus is used as both the filler wire and substrate material in this study. The chemical composition is provided in Table I. A rolled 718Plus plate is used as the substrate with dimensions of 12.5 mm x 110 mm × 45 mm, and used as-received. Deposits were made by using a tungsten inert gas (TIG) welding system integrated with a 6-DOF Panasonic VR-004 robot. The filler wire has a diameter of 1.6 mm and was fed by the wire feeder in the Panasonic robot into the arc on the substrate alloy. Argon gas was utilized for shielding the molten pool from air to prevent oxidation, which also helped to dissipate heat from the solidifying metal, thereby enhancing cooling. A considerable number of trials were initially carried out to obtain the deposition parameters to obtain a smooth and reproducible deposit with fewer visual defects. After this was achieved, a single wall of 1-, 5-, and 10-layer deposits carried out by WAAM was laid onto the substrate with the use of the deposition parameters in Table II. The total length of all of the deposits is about 70 mm, and no delays are allowed between the deposition scans.

B. *Temperature Measurement*

To monitor the thermal cycle during the deposition scans, a K-type thermocouple was resistance spot welded to the substrate before the deposition (as shown in Figure 1(b)). The thermocouple was protected from the arc with Tantalum foil with a thickness of 0.12 mm that was spot welded over the thermocouple. A 10-layer deposit was placed over the Tantalum plate and the temperature cycle during deposition was monitored and recorded with the control display.

C. *Material Characterization*

Specimens were sectioned from the deposits and mounted in a conductive Bakelite for analysis through optical microscopy (OM) and scanning electron microscopy (SEM). They were polished by using standard metallographic techniques and further subjected to chemical polishing in a Vibromet polisher with a colloidal silica suspension. They were then electro-etched with either 10 pct Oxalic acid at 5 V for 3 to 5 seconds or 170 mL of H_3PO_4 + 10 mL H_2SO_4 + 15 g CrO_3 at 5 V for 20 seconds depending on the treatment condition of the specimen. SEM was performed with a JEOL 5900 scanning electron microscope (Oxford Instruments) with an ultra-thin window energy dispersive spectrometer (EDS) and an FEI Nova NanoSEM 450 with a high-resolution field emission gun (FEG). Electron backscatter diffraction (EBSD) was conducted by using a Philips LX30 scanning electron microscope, equipped with an EDS (Oxford Instruments) and EBSD detector and analysis system. Electron microprobe analysis was conducted using Cameca SX100 Electron Microprobe equipped with Princeton Gamma Tech (PGT) Prism 2000 detector.

Thin foils used for carrying out transmission electron microscopy (TEM) were also sectioned from some of the selected regions of the deposit, grounded to about 100 μm using 400 grit sandpaper, and punched out in 3-mm

Table II. Deposition Parameters for 5- and 10-Layer Deposits

Deposition Parameters	
Arc current (A)	100
Travel speed (m/min)	0.1
Wire feed speed (m/min)	0.4
Arc length (mm)	3.0

Table I. Composition of ATI 718Plus Substrate and Filler Wire in Wt Pct

Materials	Element	Ni	Nb	Fe	Cr	W	Ti	Al	Mo	Co	C (ppm)	B (ppm)
Substrate	wt pct	52.2	5.5	9.3	17.9	1.1	0.7	1.5	2.7	9.0	40	30
Wire	wt pct	bal	5.5	9.1	17.6	1.0	0.85	1.5	3.1	9.2	40	30

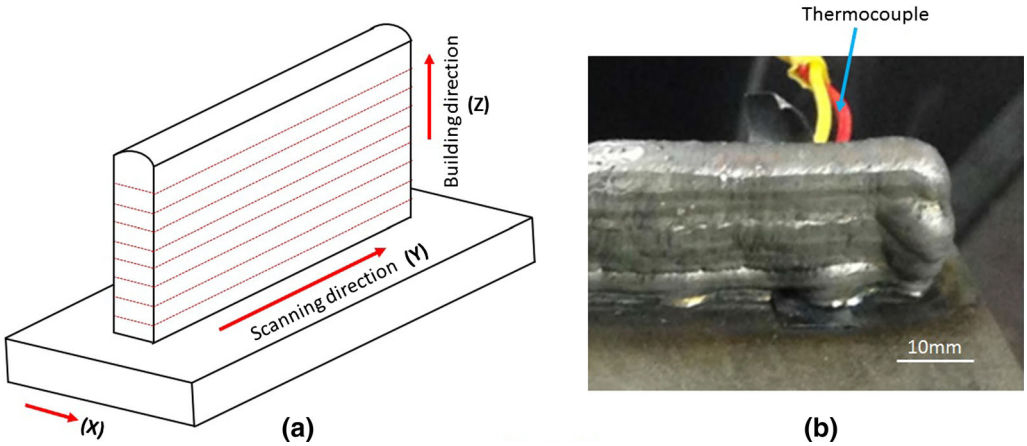

Fig. 1—(*a*) Schematic diagram of deposition showing the scanning and building directions. (*b*) ATI 718Plus build on 718Plus substrate.

coupons before subjected to dimpling and electro-polishing. The electro-polishing of the foils was carried out with a twin-jet polisher in a solution of 10 pct chloric acid + 90 pct methyl alcohol at around 233 K (−40 °C). TEM was performed on an FEI Talos F200X transmission electron microscope equipped with a Super-X EDS system with 4 silicon drift detectors (SDDs).

The hardness profile across the deposit was obtained with a Buehler microhardness tester under a load of 300 g by using the same specimen as that for the SEM.

III. RESULTS AND DISCUSSION

A. *Macrostructure and Deposit Morphology*

From the initial trials of deposition, it was observed that the morphology of the deposit is largely affected by the arc current when the wire feed rates and travel speed were constant. Figures 2(a) and (b) show a flatter and wider deposit with increasing arc current. A two-layer deposition was made as presented in Figure 3(a), and the dotted white line is the fusion line between the first deposition and the subsequent deposition scan. It can be seen that after the second deposition scan, the thickness of the first layer is significantly reduced which is attributed to the re-melting of the uppermost portion of the prior deposit which is in direct contact with the molten metal, thus becoming part of the new solidifying layer. This phenomenon is also found in all of the multi-layer deposits, as the thickness of the final deposition scan is always the greatest. After these initial trials, single wall deposits with 5 and 10 layers of 718Plus were placed onto the substrate for hardness measurement and also the microstructural analysis. The fusion lines that can be seen in the *X*–*Z* direction in Figure 3(b), and rippled surface on the exterior of the wall in Figure 1(b), indicate the deposition scans of the 10-layer deposit. The measure of these surface ripples on a deposit has been reported to depend on some of the deposition parameters and feedstock dimensions.[24,25] In this study, the diameter of the filler wire is about 1.6 mm,

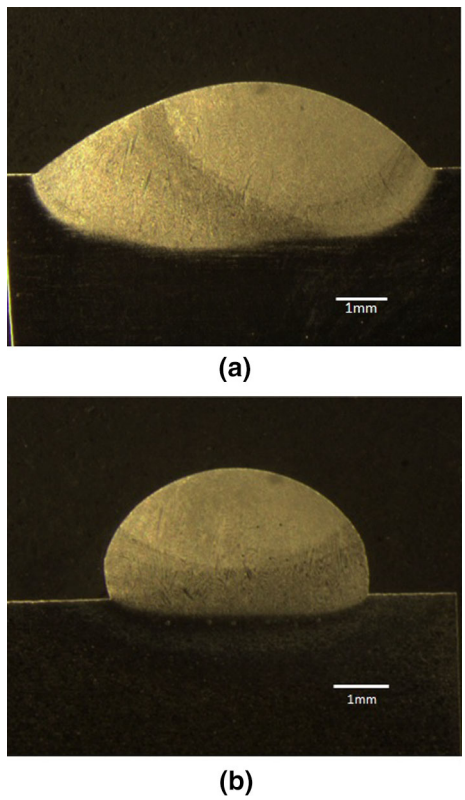

Fig. 2—Optical image showing the effect on arc current on the macrostructure of 1-layer deposits: (*a*) 130A and (*b*) 100A.

which is relatively wide and hence results in the obvious surface ripples. Aside from the surface ripples, there are no cracks, improperly fused regions, or any pores observed in any of the deposits (Figure 4).

B. *Hardness Profile of Deposit*

Figure 5 illustrates the hardness profiles of the 1-, 5-, and 10-layer deposits after carrying out the Vickers micro-indentation test. The profiles were measured along the center line of the transverse section of the

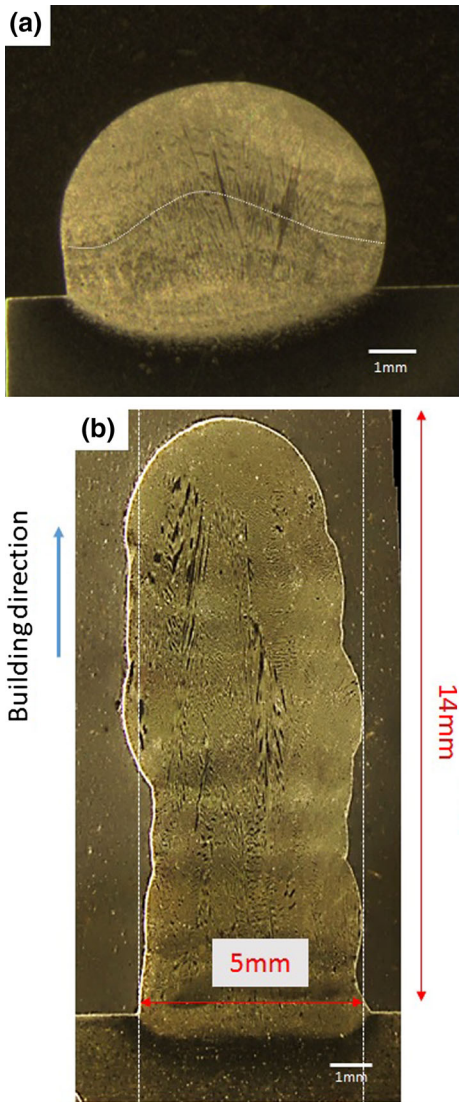

Fig. 3—Macrostructure of ATI 718Plus deposit showing (*a*) a 2-layer deposit and (*b*) a 10-layer deposit, on ATI 718Plus substrate.

build-up. There is no significant variation in the hardness of the deposits measured in the transverse (*X*–*Z*) direction and that measured along the longitudinal (*Y*–*Z*) direction. It can be observed that the hardness values for the as-solidified single-layer deposit (as-solidified zone (ASZ) henceforth) and those for the final layer of the 5- and 10-layer depositions are comparable (about 270 HV). The similarity in the hardness of these regions can be attributed to the resemblance in the solidification characteristics and also to the fact that they do not experience further thermal cycles after solidification. The bottom-middle region (denoted as the hardened zone (HZ) henceforth) has the highest hardness value (average value about 330 HV) of the deposit. In general, the size of the hardened region of the deposit from the substrate increases with increases in deposition scans. Surprisingly, the region below the ASZ which spans about 2 mm (denoted as the DMHAZ henceforth), was observed to have the least hardness (about 230 HV) in the deposit. This softened zone was also found to be transient and moves with each subsequent deposition scan as seen in the hardness profile of the deposits in Figure 5. It is worth noting that although previous studies have indicated a hardness gradient and mechanical heterogeneity in additive manufacturing deposits,[26,27] the observed softening in this work has not been reported in the additive manufacturing of 718 or 718Plus. This softening, if neglected during processing, could have serious detrimental effects on the integrity of the finished deposit in service. A similar softening, with deleterious effects on the mechanical properties, has been previously reported in the HAZ of dual-phase steel.[28] The phenomenon was recognized as HAZ softening, and first identified when dual-phase steels were flash butt welded for wheel rim applications.[29] It was found that failure consistently occurs at the prior softened HAZ, which is caused by the tempering of martensite in the HAZ during the welding process. It is thus, imperative to have a proper understanding of the underlying mechanism of this observed softening in the deposit. Therefore, our main focus is to study the mechanism behind this softening.

C. *Temperature Evaluation During 10-Layer Deposition*

To analyze the phase transformation during the deposition of 10 layers of 718Plus, the thermal profile during scanning is an important factor which needs to be examined. To do so, the temperature measurement method in Segerstark[30] is modified in this study, as discussed in the experiment and method section. The solid black line in Figure 4(a) shows the temperature measurement by the thermocouple at the bottom of the 10-layer deposit. Placement of a thermocouple within the build to monitor the thermal cycle during scans was not feasible. Therefore, thermal values in the build were estimated by using the thermal history from the bottom of the build. The estimated temperatures for the 6th layer (middle region of the deposit) and the 9th layer of the deposit (the DMHAZ) are also presented as a dotted line in Figure 4(a). The blue dotted line denotes the approximate range of the aging temperature for the precipitation of γ'/γ'' as seen in the calculated time temperature transformation (TTT) diagram in Figure 12. Figure 4(b) shows the temperature frequency distribution plot of the zones from the deposit. The bottom and middle zones of the deposit are observed to have spent considerable time in the aging temperature range during scanning, hence significant precipitation and strengthening are expected. In addition, the temperature at the DMHAZ (or 9th layer) during the final deposition scan is over 1373 K (1100 °C) which exceeds the solvus temperature of the strengthening precipitates (γ'/γ'' precipitates). Therefore, if any strengthening precipitates were formed during the solidification of this zone, they are anticipated to have completely dissolved during the final deposition scan.

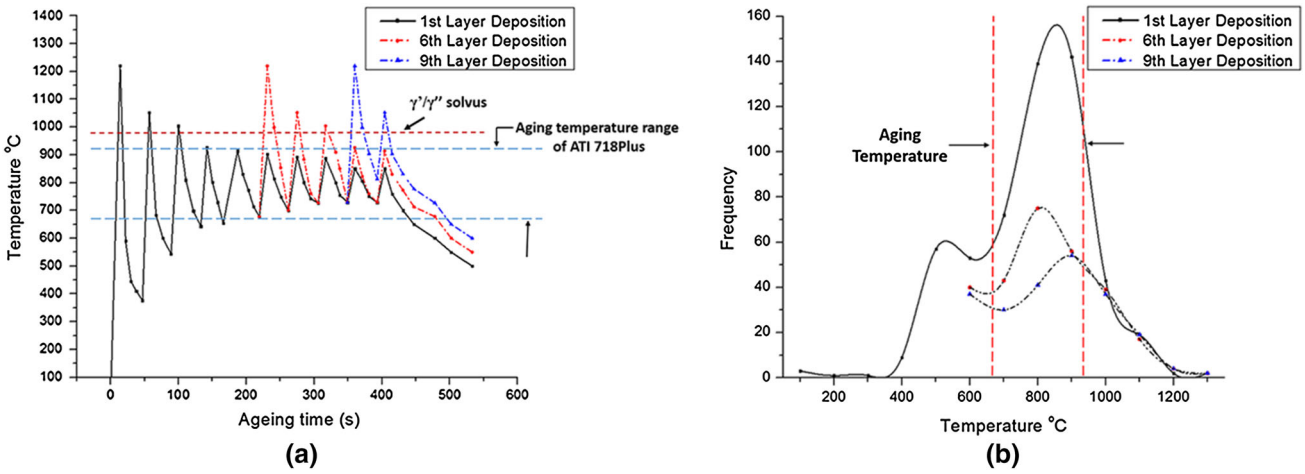

Fig. 4—(*a*) Temperature profile of the deposit at different locations in the build and (*b*) estimated frequency distribution of temperature of the 1st, 6th, and 9th layer depositions.

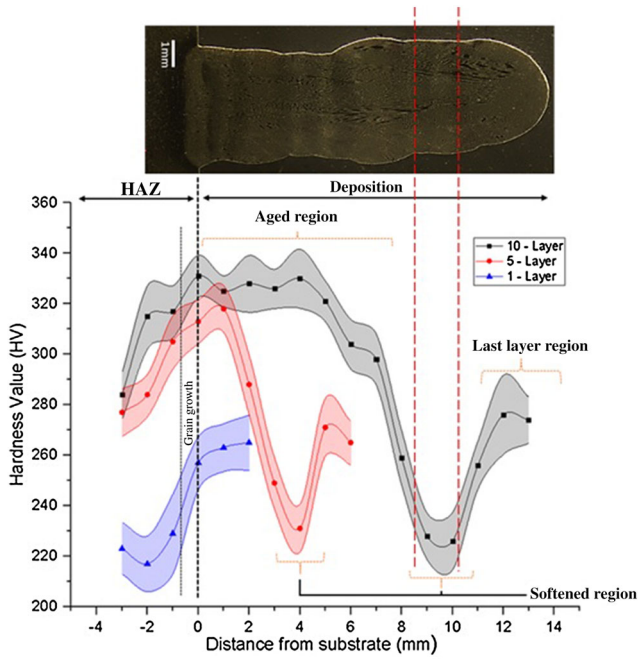

Fig. 5—Hardness profile of the 1-, 5-, and 10-layer depositions.

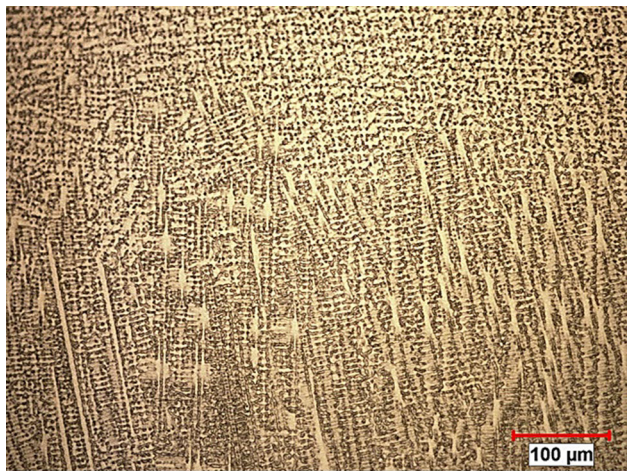

Fig. 6—Optical micrograph showing the solidification microstructure of a single-layer deposit.

D. *Microstructure*

1. *Characterization of single-layer deposition*

An essential prerequisite to defining the fundamental cause of softening is a proper understanding of the solidification characteristics and solid-state transformation during the single-layer deposition of 718Plus. An optical micrograph of a single-layer deposit is shown in Figure 6. The micrograph shows a structure with columnar and equiaxed dendritic solidification, in which the columnar structure is at the bottom in the direction of the heat extraction, while the equiaxed structure is at the top. The fine equiaxed structure at the top may be due to the considerable cooling effect from the shielding gas. An examination of the deposit by using a scanning electron microscope at higher magnification shows that there are some secondary phase particles in the interdendritic regions, see Figure 7(a). The majority of the particles are irregular in shape, distributed discretely along the interdendritic regions. Associated with these irregular-shaped particles are some blocky-shape particles. The preliminary SEM/EDS analysis on these secondary constituents showed that they are enriched with Nb. A similar microstructure was reported in the solidified fusion zone of the welded 718Plus[7,23,31] and in AM of IN 718.[32] The morphology of these particles, their location, and composition suggest that they are based on the Laves phase and MC type of carbides. Furthermore, the SEM backscatter image in Figure 7(b) shows a bright compositionally contrasting ring around these interdendritic particles, which suggests that these bright regions contain higher atomic elements. A high-resolution scanning electron microscope with FEG was used to examine the microstructure of these bright regions (presented in Figure 7(c)). A dense population of nano-sized precipitates were observed around the secondary phase constituents and also in

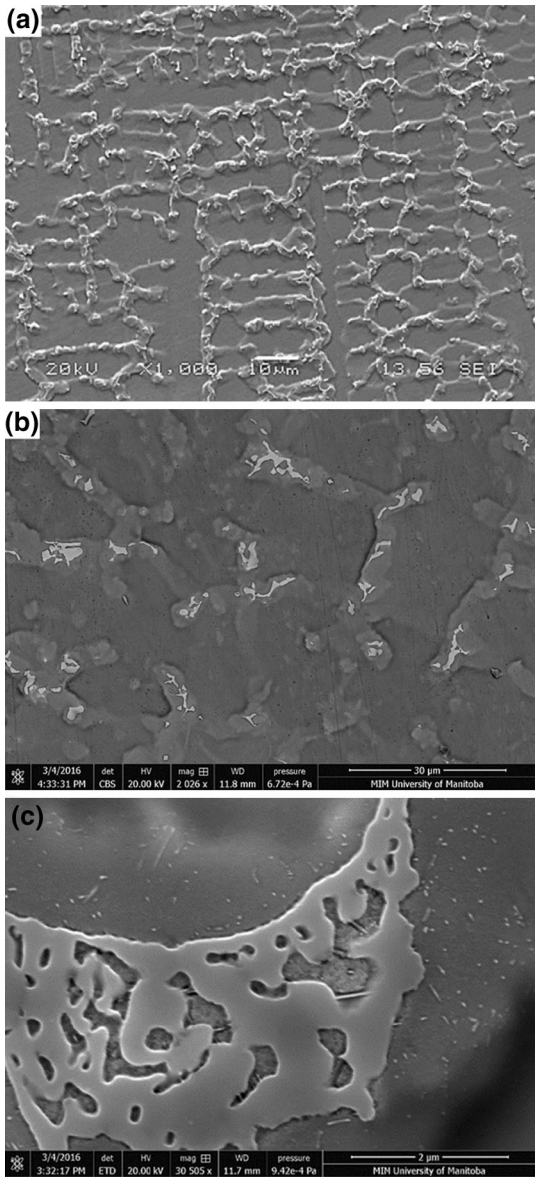

Fig. 7—SEM micrographs of single-layer deposited ATI 718Plus showing (*a*) eutectic solidification microconstituents in the interdendritic regions, (*b*) bright contrast rings along the interdendritic regions, and (*c*) high magnification image of nano-scaled interdendritic particles.

other areas of the interdendritic regions. However, the majority of these precipitates are fine in shape and the details cannot be resolved. They could be the strengthening precipitates found in 718Plus that are reported to be the γ' and γ'' precipitates.

Aside from our previous study on the TIG welding of 718Plus,[23] the formation of strengthening precipitates has not been commonly reported during the solidification of 718Plus welds. Besides these strengthening precipitates, plate-like particles were also observed in the interdendritic regions. The morphology of these particles suggests that they are either the δ or η phase particles often reported in the grain boundaries of 718Plus but in this case, they are precipitated in the interdendritic regions.

TEM was carried out to examine the structure and composition of the secondary constituents in the interdendritic regions, and resolve and verify the properties of the associated precipitates. Figure 8 shows a TEM bright-field image and the selected area diffraction patterns (SADPs) of the blocky-shape particles observed in the interdendritic regions. Details of the TEM/EDS analysis are summarized in Table III, which show that the particles have a high Nb content with a significant amount of Ti. The SADPs of the [001], [110], and [130] zone axes presented in Figures 8(b) through (d), respectively, indicate that the crystal structure is a cubic NaCl-type structure with a lattice parameter $a = 0.45$ nm. From the EDS analysis and the SADP, it can be concluded that these particles are composed of Nb, Ti-rich carbides (NbC). Similarly, a TEM bright-field image of the other irregular shape particles in the interdendritic region and the SADP of the $[1\bar{1}00]$,$[10\bar{1}0]$, and $[2\bar{2}03]$ zone axes are shown in Figure 9. The TEM/EDS carried out on these particles shows that they contain a relatively high content of Nb, chromium (Cr), Ni, Fe, and other minor elements that have a composition close to $(Ni, Cr, Fe)_2(Nb, Mo, Ti)$ at. pct as listed in Table III. Also, the SADPs in Figures 9(b) through (d) show that these particles have a hexagonal crystal structure with a lattice parameter $a = 0.48$ nm and $c = 0.78$ nm. The TEM analysis confirmed that these irregular particles are based on the Laves phase. The presence of Laves phase has not be previous reported in 718Plus produced by additively manufactured process.[19,20] However, it is generally known that the presence of Laves phase particles in 718Plus is detrimental to its mechanical properties. Thus, this study has shown that, there is the need to develop new heat treatment procedure to eliminate or reduce the presence of Laves phase particles in the deposit to optimize the properties.

To analyze the strengthening precipitates observed in the interdendritic region, TEM analysis was performed on the SADP in the [100] zone axis of the γ matrix and presented in Figure 10(a). Superlattice reflections that correspond to γ' and γ'' can be observed in the interdendritic regions with proximity to the secondary phase constituents. The bright-field image of the interdendritic region in Figure 10(c) shows the strengthening precipitates but due to the high coherency with the matrix, the γ' precipitates are barely visible. A dark-field (DF) image of the γ'' precipitates in Figure 10(d) shows that the average length and width of the γ'' precipitates along the interdendritic region is about 20 nm and 5 nm, respectively. Also, the DF image of the (001) reflection in Figure 10(e) shows the average size of the γ' precipitates to be about 10 nm. White streaks can be observed to be associated with the γ' precipitates, which could have been from the γ'' reflections, thus suggesting that there could be associated precipitation of the γ' and γ'' precipitates. Xie *et al.*[33] and Cozar[34] reported similar associated precipitation of γ' and γ'' precipitates in modified IN 718. They attributed the precipitation behavior to the content and ratio of Nb, Ti, and Al in the Ni alloy. Elemental micro-segregation during

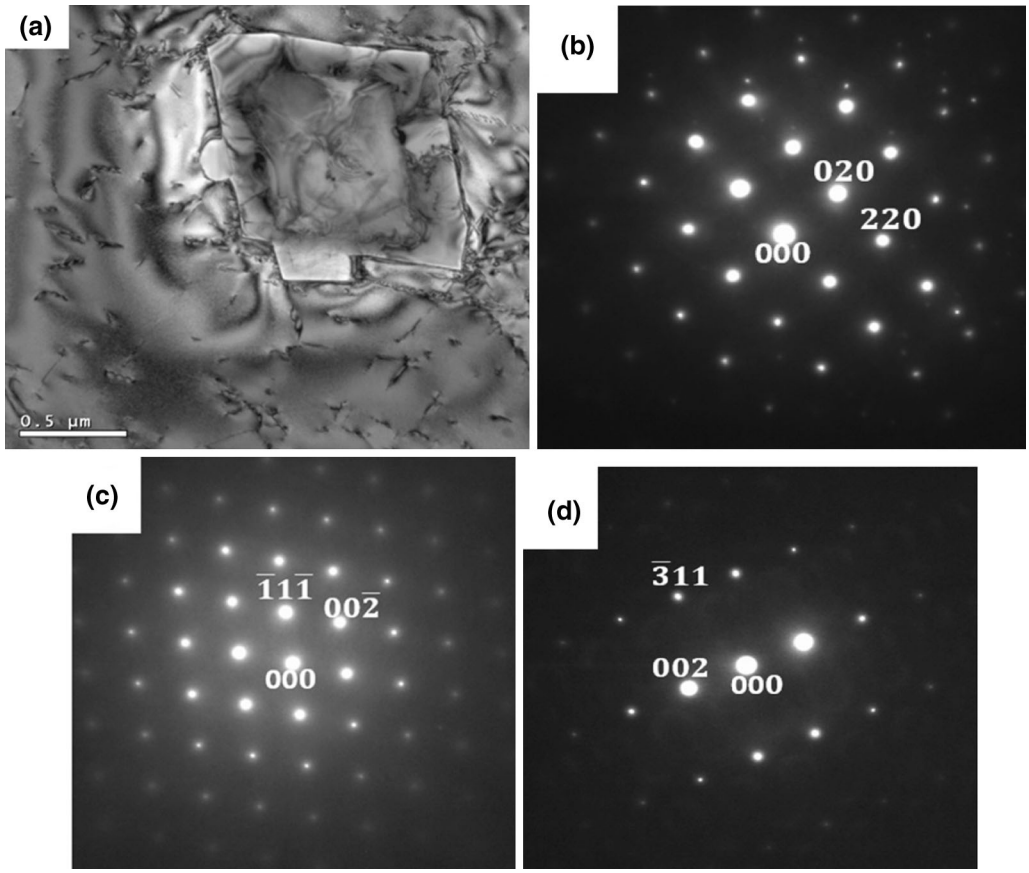

Fig. 8—TEM analysis of single-layer deposited ATI 718Plus showing (*a*) bright-field (BF) image of NbC, and the selected area diffraction patterns (SADPs) from (*b*) [001], (*c*) [110], and (*d*) [130] zone axes of the carbide.

Table III. EPMA/WDS Point Analysis of Interdendritic Regions of the Deposit, and TEM/EDS of Laves Phase and MC Carbide Particles

	EPMA/WDS Point Analysis of Interdendritic Regions Deposit					TEM/EDS of Laves Phase and MC Carbide	
		As-Solidified Interdendritic		DMHAZ Interdendritic			
	Elements	Wt Pct	At Pct	Wt Pct	At Pct	Laves Phase Wt Pct	MC Carbide Wt Pct
1.	Ni	50.5	51.0	51.2	51.2	40.7	7.1
2.	Al	1.3	2.9	1.4	3.0	0.7	0.1
3.	Co	8.8	8.8	8.9	8.8	8.2	1.2
4.	Cr	16.3	18.6	17.4	19.1	14.0	5.0
5.	Fe	8.6	9.1	9.1	9.5	7.1	1.9
6.	Mo	3.3	2.0	3.0	1.8	3.5	2.9
7.	Nb	9.2	5.8	7.2	4.3	23.5	70.1
8.	Ti	1.1	1.3	1.0	1.2	1.0	11.7
9.	W	0.8	0.3	0.9	0.3	0.7	0.2

solidification may have influenced the concentration of these elements in the interdendritic regions, thus prompting the formation of the observed associated precipitates. Furthermore, most of the strengthening precipitates are concentrated along the interdendritic regions, and are reduced with increasing distance from the interdendritic regions. Inside the dendrites, only γ' precipitates formed in the regions close to the interdendritic regions without the γ'' precipitates as seen in the SADP in Figure 10(b), while no evidence of either γ' or γ'' precipitates was observed within the dendrite core. The observed strengthening precipitates in the interdendritic regions of the as-solidified deposit could have somewhat strengthened the deposit.

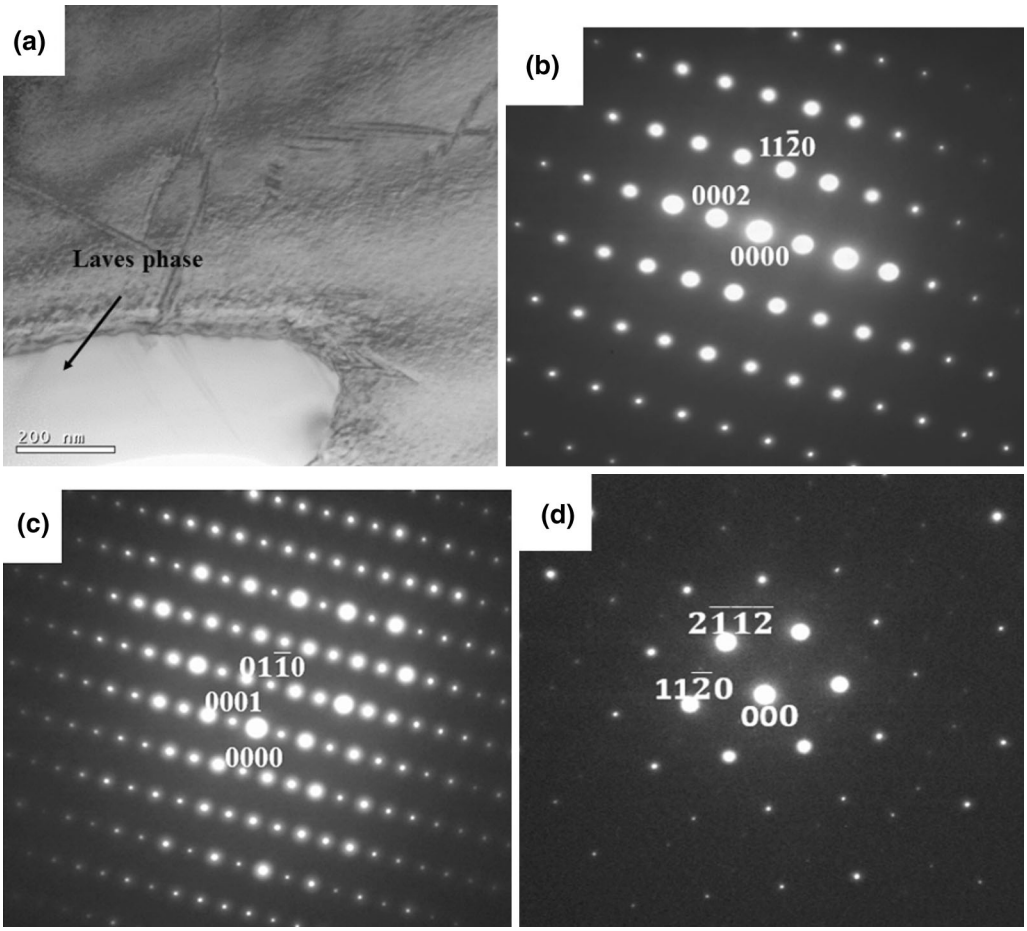

Fig. 9—TEM analysis of single-layer deposited ATI 718Plus showing (*a*) BF image of Laves phase, and the SADPs from (*b*) $[1\bar{1}00]$, (*c*) $[2\bar{1}\bar{1}0]$, and (*d*) $[2\bar{2}03]$ zone axes of the Laves particle.

a. Solidification characteristics and elemental micro-segregation. To explain the non-uniform accelerated precipitation and the formation of secondary constituents along the interdendritic regions, the solidification characteristics of 718Plus need to be well understood. The solidification behavior of cast 718Plus and the weld fusion zone of 718Plus has been previously investigated.[7,9,27] During the solidification of 718Plus, the primary γ-dendrite is the first solid to appear. As this dendrite grows, solute elements such as Nb and Ti with partition coefficient $k < 1$[7,23] are ejected into the liquid, which is the reason for their increased concentration in the interdendritic liquid (Figure 11). After a while, with the increasing growth of γ-dendrites, the solubility of these solute element in the interdendritic liquid is increased, thus promoting the onset of the formation of secondary phase constituents. Due to the enrichment of the interdendritic liquid with Nb and Ti, which are strong carbide forming elements, MC-type carbides eventually form through a non-variant eutectic reaction at about 1565 K (1292 °C).[7,9] The formation of MC-type carbides depletes the interdendritic liquid of most of its carbon content[35]; however, the liquid continues to be enriched with Nb as the γ-dendrites further increase. At the final stage of the solidification, the Nb content in the interdendritic liquid would have increased to about 19.7 wt pct (as shown in Figure 11) which exceeds the supersaturation limit of Nb in the liquid,[9] thus triggering the formation of Laves phase particles also by a non-variant eutectic reaction reported to occur at about 1446 K (1173 °C).[9]

b. Accelerated precipitation of strengthening phase. As discussed earlier, the segregation of Nb takes place in the interdendritic liquid during solidification thus leading to the formation of secondary phase constituents. The γ matrix around the interdendritic regions is expected to be enriched with Nb compared to the γ matrix in the dendrite core, and this can be observed in the SEM backscatter image in Figure 7(b). The EPMA/wavelength-dispersive spectroscopy (WDS) analysis presented in Table III shows that the γ matrix in the interdendritic regions has a higher content of Nb of about 9.2 wt pct which is in agreement with the solubility limit of Nb in the γ-matrix [at 1446 K (1173 °C)] as shown in the pseudo-binary phase diagram of 718Plus developed by Cao *et al.*[9] The accelerated precipitation of the strengthening precipitates observed in the interdendritic regions can be attributed to the increased Nb content which contributes to their

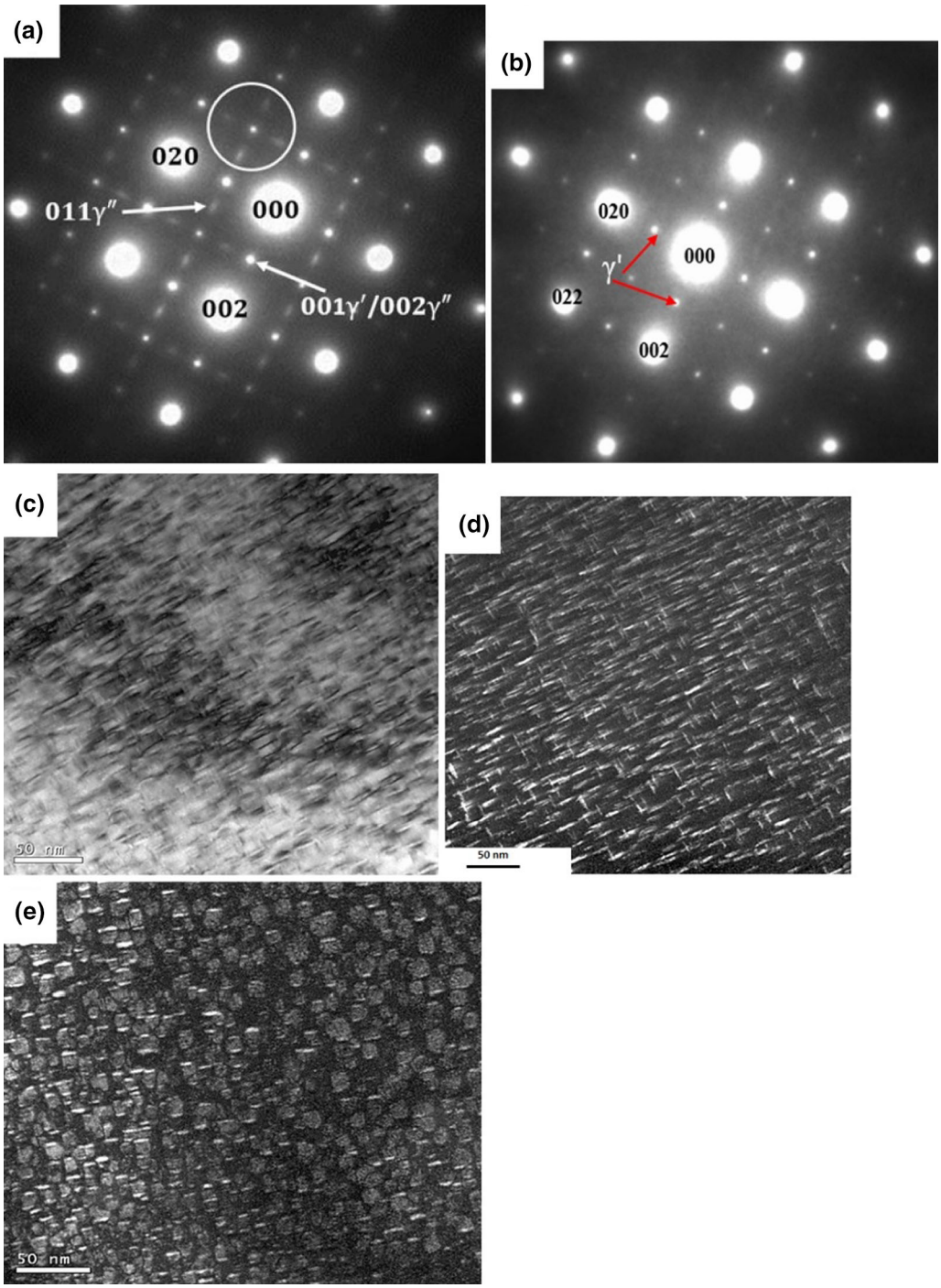

Fig. 10—TEM analysis of single-layer deposited ATI 718Plus: (*a*) SADP from the interdendritic region showing the superlattice reflection from γ' and γ'' precipitates, (*b*) SAD pattern from the interdendritic/dendritic core boundary showing the reflections from only γ' precipitates, (*c*) BF image of strengthen precipitates in the interdendritic regions, and (*d*) dark-field (DF) image of γ'' taken from the encircled diffraction spots in (a), and (*e*) dark-field image of γ' and γ'' precipitates taken from the (001) reflection in (a).

formation. To validate this assertion, a TTT-diagram of an Nb-enriched γ-matrix is constructed by using Java-based materials properties software (JMatPro) and compared with that constructed from nominal 718Plus as presented in Figure 12. It is apparent from the plot that the kinetics of the precipitation of the γ'/γ'' precipitates is faster with higher Nb content. This is in agreement with our earlier study where we observed that the segregation of Nb during welding affects the kinetics of precipitation of the strengthening phase in 718Plus.[23] Also, contrary to the precipitation characteristic of 718Plus,[9] the kinetics of γ'' seems to be faster than that

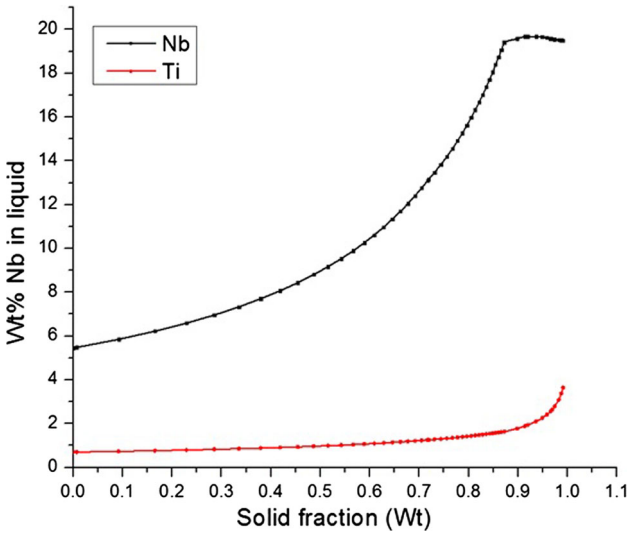

Fig. 11—JMatPro simulation showing the partitioning of Nb and Ti at the liquid–solid interface.

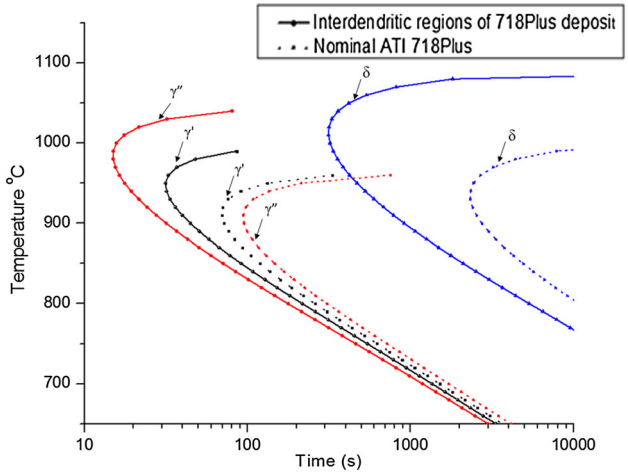

Fig. 12—Calculated TTT curve for γ', γ'', and δ-phase precipitates of ATI 718Plus and modified ATI 718Plus (from the interdendritic regions) using JMatPro software.

of γ' in the interdendritic region as presented in the constructed TTT plot in Figure 12. The higher content of Nb with the significant change in the chemistry of the interdendritic region due to segregation may be responsible for this seemly change in the precipitation order of the strengthening precipitates. In previous studies, Cozar *et al.*[34] and Xia *et al.*[33] reported that when the ratio of Al + Ti at pct to Nb at pct is greater than 0.8, the precipitation of γ' precedes that of γ'' in Ni-based superalloys. Sundararaman *et al.*[36] concluded that in 718 superalloys (with (Al + Ti)/Nb ~ 0.6), the precipitation of γ' does not seem to precede γ'' precipitation. In a more recent study by Alam *et al.*,[37] on the early stages of the aging of IN 718 (with (Al + Ti)/Nb ~ 0.7), they found out that γ'' precipitation precedes that of γ' precipitation. Nalawade *et al.*,[38] however, showed that a local increase in (Al + Ti)/Nb ratio (to about 1.4) in 718, due to prior heat treatment, can reverse this precipitation sequence. In this study, Al + Ti at. pct to Nb at. pct at the interdendritic region was estimated to be around 0.71, which is obviously less than 0.8 as suggested by Cozar *et al.*[34] as the point of reference for change in the precipitation sequence and may be the reason for the observed change in the calculated precipitation order at the interdendritic regions.

2. *Microstructure of multi-layer deposition*

a. Liquation and re-solidification of γ/laves eutectics. In the previous section, the typical solidification microstructure and solid-state transformation of the first deposited layer of 718Plus during WAAM are discussed (which is comparable to the solidification microstructure of every subsequent deposited layer). Upon subsequent deposition scanning, the prior layer acts as the substrate to the subsequent depositions and is affected by the heat from the molten pool of the new deposition. The top part of the earlier deposit which is in contact with the molten pool is re-melted and becomes part of the new deposit as described earlier. The regions below the top layers with temperatures that are not high enough to melt the bulk alloy but high enough to liquefy the low melting eutectics (such as the γ/Laves eutectics) cause some of the eutectic particles to dissolve into the surrounding γ-matrix and the majority of the particles to liquefy as shown in Figure 13(a). The liquid Laves phase reforms as continuous long chain particles and in some cases, along the grain boundaries of the deposit as shown in Figure 13(b). A similar microstructure in IN 718 after AM[39,40] and HAZ of 718Plus[7,31] shows that these metallurgical features promote the initiation and propagation of liquation cracking. In this study, notwithstanding the presence of these metallurgical features in the DMHAZ, no cracks are observed in the deposit. This could be resultant of the amount of induced strain acting on the liquated Laves phase during re-solidification. It has been suggested[41] that there is relatively less thermal stress generated in the HAZ during high heat input welding-like the modified TIG system used in this study. Induced thermal stress in the HAZ has been recognized[6,31] as a key factor that influences liquation cracking in the welding of 718Plus and cracking can be minimized by utilizing a high heat input deposition process.

b. Grain morphology and textural characteristics of deposit. An EBSD analysis was carried out to examine the grain morphology and the texture of the build due to the re-melting that took place during the deposition scans. The inverse pole figure (IPF) of the top and bottom/substrate of the transverse cross-section (X–Z direction) of the deposit is presented in Figures 14(a) and (b), respectively. It can be observed in Figure 14(b) that fine equiaxed grains with a thickness of a few microns are formed around the substrate/deposit interface. The observed fine grains could be attributed to the

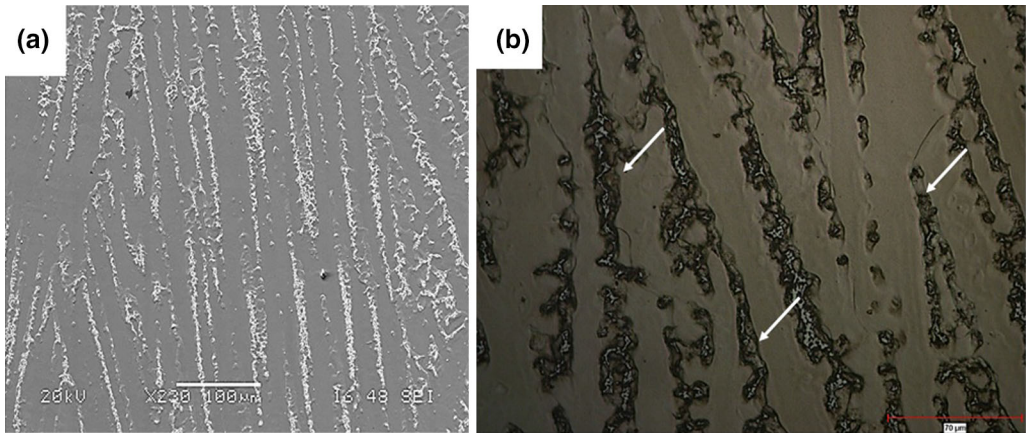

Fig. 13—(*a*) SEM micrograph showing the re-solidification of continuous Laves phase in the deposit after subsequent deposition scan and (*b*) OM micrograph showing some resolidified Laves phase along the grain boundaries.

rapid cooling rate of the first deposit on the substrate. However, further up into the build, the grains are much coarser and columnar, oriented in the direction of the heat flow. These grains are observed to grow across the layers of the deposited scans, which may be due to the epitaxial growth that took place in the preferred growth direction. A high thermal gradient at the liquid/solid interface at low solidification velocity is recognized[21,42] as the necessary conditions for the observed epitaxial growth and these conditions have been likely achieved during the wire-arc deposition of 718Plus in this work. Moreover, it is well established that FCC crystals have the fastest growth during solidification in the <100> direction. As a result, it can be observed from the IPF that even though the grains at the bottom of the build around the substrate–deposit interface are randomly oriented, only grains with their <100> direction nearly parallel to the build direction are favored to grow rapidly, while the growth of the other grains that are not favorably oriented is truncated. This is the reason why most of the grains in this build are highly textured in the <100> directions as seen in the IPF in Figure 14. Furthermore, in the substrate (as shown in Figure 14(b)), about 250 μm below the substrate/deposit interface, there is significant grain growth. The grains in this region have grown from <20 μm to about 50 to 70 μm in size. This may be attributed to the dissolution of the grain boundary pinning particles during the deposition scans, as described in the work of Ding *et al.*[21] The temperature measured on the substrate during the first scan in this work, was observed to be above the solvus of the δ/η particles in 718Plus.[9] This likely caused the grain boundary particles close to the substrate to dissolve during the first few deposition scans thus allowing for grain growth.

The EBSD analysis provided in Figure 14 shows highly textured grains in the build direction. Although this may not be related to the observed softening in the build, it also carries a potentially detrimental effect due to the possibility of anisotropy of the mechanical properties of the deposited material.

c. Analysis of strengthening precipitates in the multi-layer deposit. The solid-state transformation and formation of strengthening phases in the HZ and DMHAZ softening due to the thermal gyrations during deposition scans was studied. A SEM high-resolution micrograph from the interdendritic region of the DMHAZ is presented in Figure 15(a). Although not resolvable from the micrograph, the white contrast regions around the Laves phase particles suggest that small-sized precipitates are likely present along the interdendritic region of this zone. A TEM analysis was carried out to confirm the presence and characteristics of these precipitates. The SADP obtained through TEM of the [100] zone axis of the γ matrix taken from the white contrast regions around the Laves phase particles is presented in Figure 15(c). The diffraction shows the superlattice reflections of both γ' and γ'' precipitates, which confirms their presence close to these secondary constituents along the interdendritic regions of the DMHAZ.

However, moving away from these secondary constituents toward the dendrite interior, only weak γ' superlattice reflections are present at the dendrite boundary, and within the dendrite core itself, no γ'/γ'' reflections are observed. From the BF and DF images obtained by TEM in Figure 15(b) and (d) respectively, the average length of the γ'' precipitates in the interdendritic region of the DMHAZ is about 5 to 7 nm, while the DF image in Figure 15(e) shows the average diameter of the γ' precipitates to be <5 nm. These estimated precipitate sizes in the DMHAZ are significantly smaller than the average size of the γ'/γ'' precipitates observed earlier in the ASZ. A typical high-resolution SEM micrograph of the bottom region of the deposit is presented in Figure 16(a). As discussed earlier, this region of the deposit is exposed for a considerable amount of time to the aging temperature range of the alloy thus promoting the nucleation and growth of precipitates. The spherical morphology of the precipitates in the micrograph indicates that the γ' precipitates are the dominant strengthening phase. Larger precipitates are found at the interdendritic

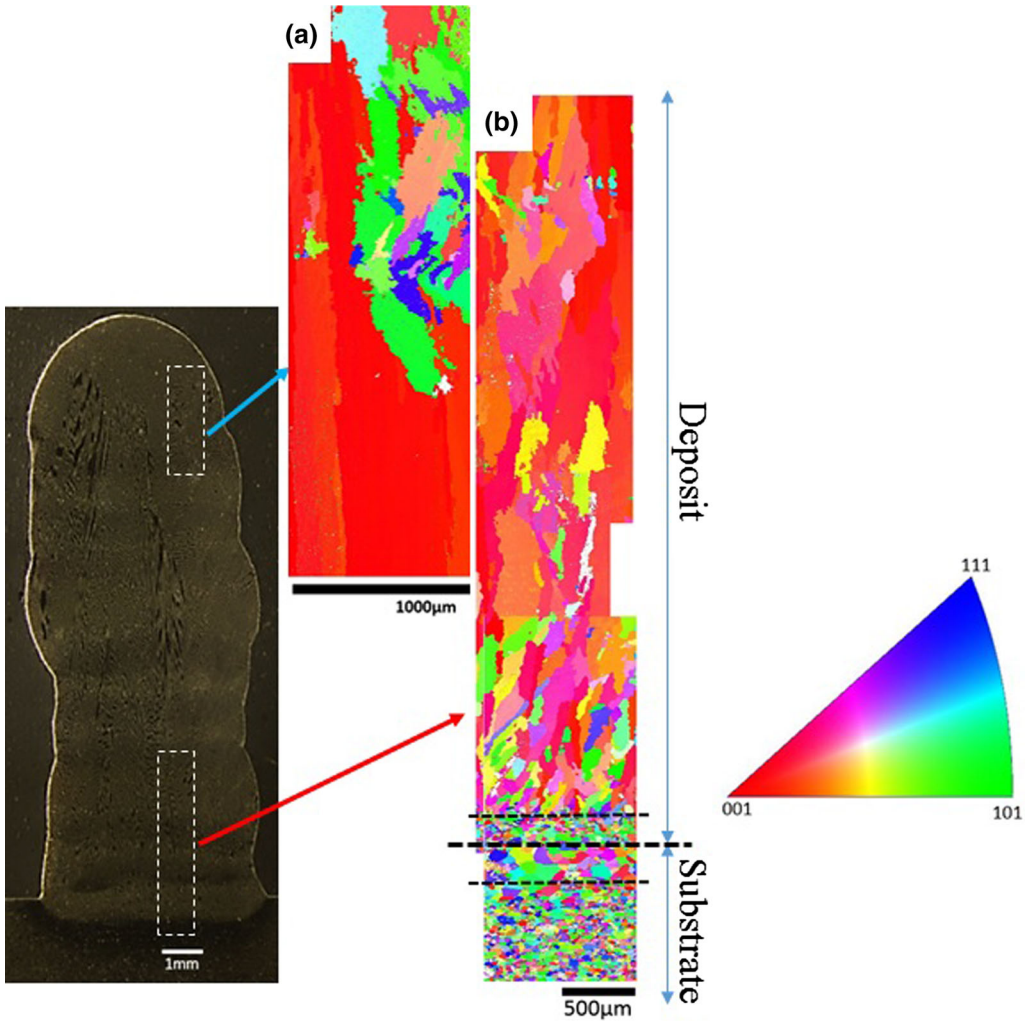

Fig. 14—IPF-based orientation maps obtained from the 10-layer deposited ATI 718Plus showing (*a*) few misoriented grains at the top of the deposit and (*b*) highly textured grains at the bottom of the deposit with only fine misoriented grains at the deposit/substrate boundary.

regions near the secondary constituents which become smaller in size with distance from the dendrite core. Although strengthening phases are also expected within the dendrite core due to the increased aging time, the details of the precipitates are not resolved in the SEM image, likely due to their small size. The SADP obtained by carrying out TEM of the [100] zone axis of the γ matrix in the interdendritic regions of the deposit showed superlattice reflections from both the γ' and γ'' precipitates. However, in the dendrite core, there is only the reflection of the γ' precipitates. The γ' precipitates along the interdendritic region are as large as 25 to 30 nm in size, and those in the dendrite cores are estimated to be around 5 nm as seen in Figures 16(b) and (c), respectively. This spatial variation of the precipitates, across the deposit, can be attributed to the varying concentrations of Nb in the deposit, which likely affects the precipitation kinetics.

d. Quantification of strengthening precipitates. Due to the spatially varied strengthening precipitation within the build, a two-step analysis was carried out to estimate the precipitation in the different zones: (i) the area fraction of the regions where precipitation is likely is first estimated with a SEM micrograph at low magnification, and then (ii) the area fraction of the nano-precipitates in these regions is then determined from high-resolution SEM and TEM micrographs. A similar method was used by Makiewicz *et al.*[43] who examined solid-state transformation in 718. The longitudinal sections of the deposit from the ASZ, DMHAZ, and the HZ were utilized for the quantification.

Table IV is a summary of the estimated area fractions of precipitates from the different zones of the deposit. It is evident that the overall area fraction of the strengthening precipitates in the DMHAZ, which is about 3.4 pct, is the smallest of all the three zones analyzed. The ASZ with an estimated area fraction of 6.5 pct is almost twofold that of the DMHAZ. The bottom region of the deposit gives the highest estimated area fraction of the precipitates in the deposit of about 18.2 pct. It is known that the overall strengthening achieved in 718Plus, is influenced by the size and volume fraction of the strengthening precipitates, γ'/γ''. Therefore, it can be

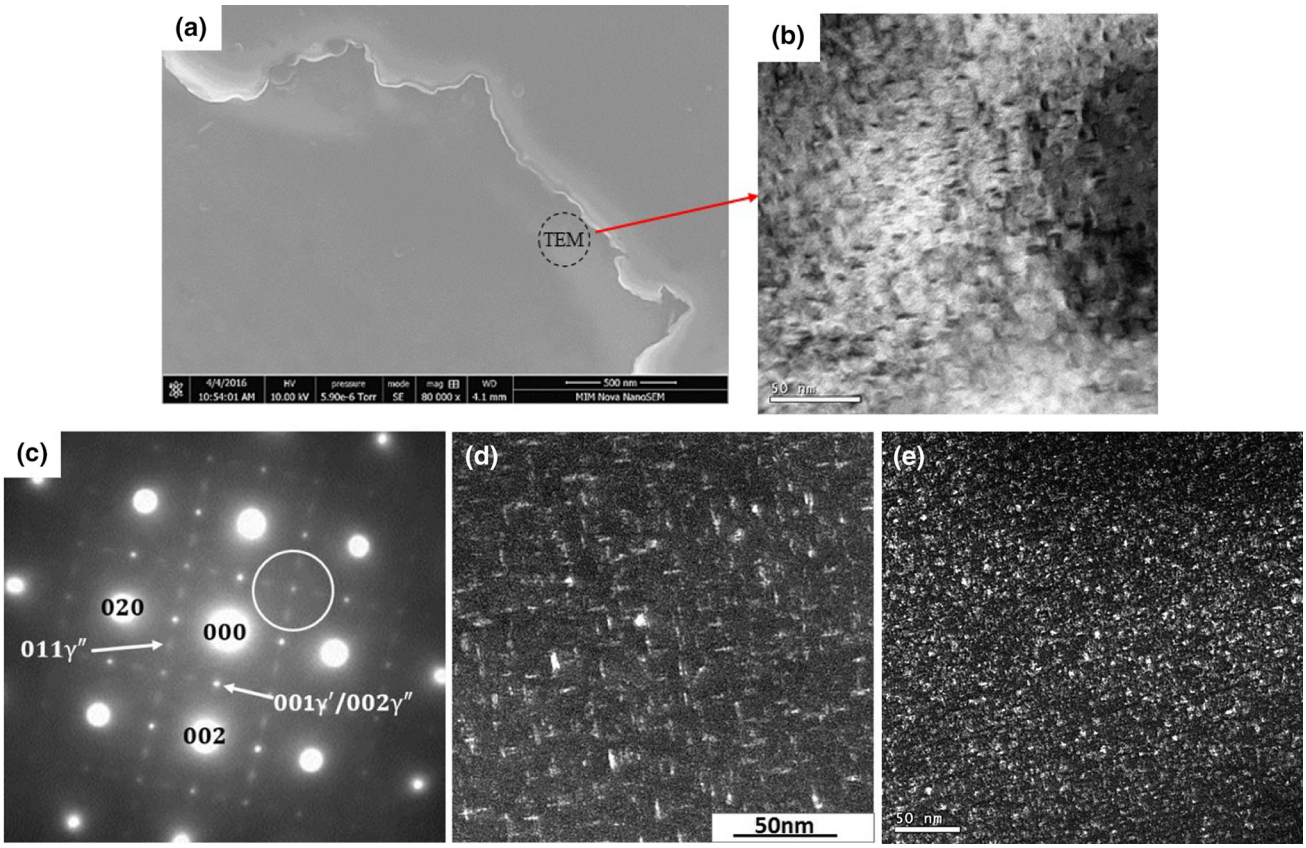

Fig. 15—(*a*) High-resolution SEM micrograph from the DMHAZ showing very fine strengthening precipitates around the Laves phase particles. TEM analysis from the interdendritic region around the Laves phase particles in the DMHAZ showing (*b*) BF image of strengthening precipitates, (*c*) SADP showing the superlattice reflections from γ' and γ'' precipitates, and (*d*) DF image of γ'' precipitates from the encircled diffraction spots in (c), and (*e*) DF image of γ' precipitates using (001) reflections.

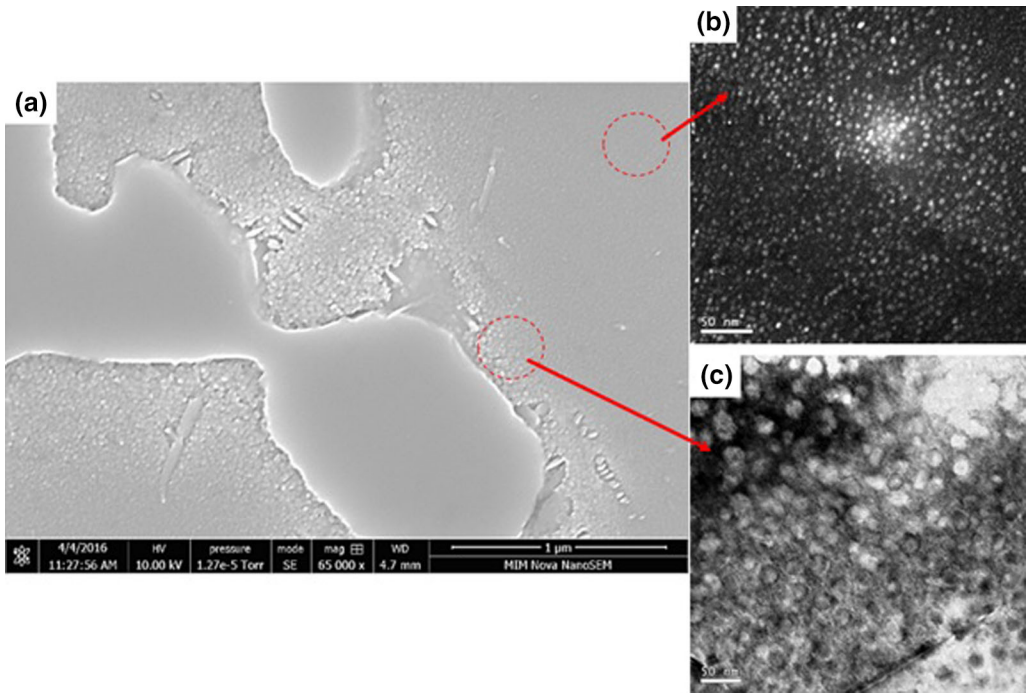

Fig. 16—(*a*) High-resolution SEM micrograph of the HZ (bottom region) of the deposit. TEM micrographs showing (*b*) DF image of finer γ' precipitates in the dendrite core and, and (*c*) BF image showing larger γ' precipitates in the interdendritic regions.

inferred that, the softening observed in the DMHAZ is attributed to the small sizes and the low fraction of strengthening precipitates in the zone. The next step is to justify the uniqueness of this softening phenomenon to the DMHAZ.

E. *Rationalization of Softening Mechanism in the DMHAZ*

1. *Diffusion of segregated solute elements in the DMHAZ*

Changes in the local concentration of segregated solute elements in the DMHAZ as a result of each subsequent scan is evaluated with an EPMA. The elemental mapping of the Nb distribution, in the ASZ and the DMHAZ (from the *X*–*Y* direction) of the deposit, is presented in Figures 17(a) and (b), respectively. Also the quantitative point analysis data carried out by WDS are listed in Table III for their respective interdendritic regions. It is evident from the elemental mapping in Figure 17(b) that there is a significant decline in the concentration of Nb along the interdendritic region of the DMHAZ compared to that obtained after solidification in Figure 17(a). This could be due to the diffusion of Nb away from the interdendritic region into the dendrite core as a result of the high concentration gradient of the Nb in the deposit.

Moreover, it is reported that the diffusion of Nb in a highly alloyed Ni-based superalloys is temperature dependent, and Nb diffuses much faster in Ni-based superalloys at temperatures above 1373 K (1100 °C)[44,45] which is the temperature that the DMHAZ likely experienced during the subsequent deposition scan. These could be the reasons for the significant reduction in the concentration of Nb in the interdendritic region of the DMHAZ after the subsequent deposition scan.

2. *Delayed re-precipitation of γ′/γ″ in the DMHAZ*

The strengthening precipitates formed in the DMHAZ during solidification presumably dissolved during the subsequent scan, as discussed earlier. Following the slow rate of cooling [about 278 K/s (5 °C/s)], these strengthening precipitates are reformed, albeit with a different precipitation kinetics. JMatPro simulation was carried out to understand the effect of the changes to the composition on the precipitation behavior in the interdendritic region, for both the ASZ and DMHAZ of the deposit. The compositional data from the EPMA are summarized in Table III and assuming

Table IV. Estimated Area Fraction of Three Zones of the Deposit

		Percent Area Fraction			
Zone	Region	Site of Precipitation Concentration (Pct)	Strengthening Precipitates from the Site (Pct)	Strengthening Precipitates from Each Region (Pct)	Total Percent Area Fraction
Bottom Zone	interdendritic regions	44.8	22.2	9.9	18.2 pct
	dendrite core	55.2	15.1	8.3	
DMHAZ	interdendritic regions	32	10.5	3.3	3.37 pct
	dendrite core	0	0	0.0	
AS-Zone	interdendritic regions	31.0	21.1	6.5	6.5 pct
	dendrite core	0	0	0.0	

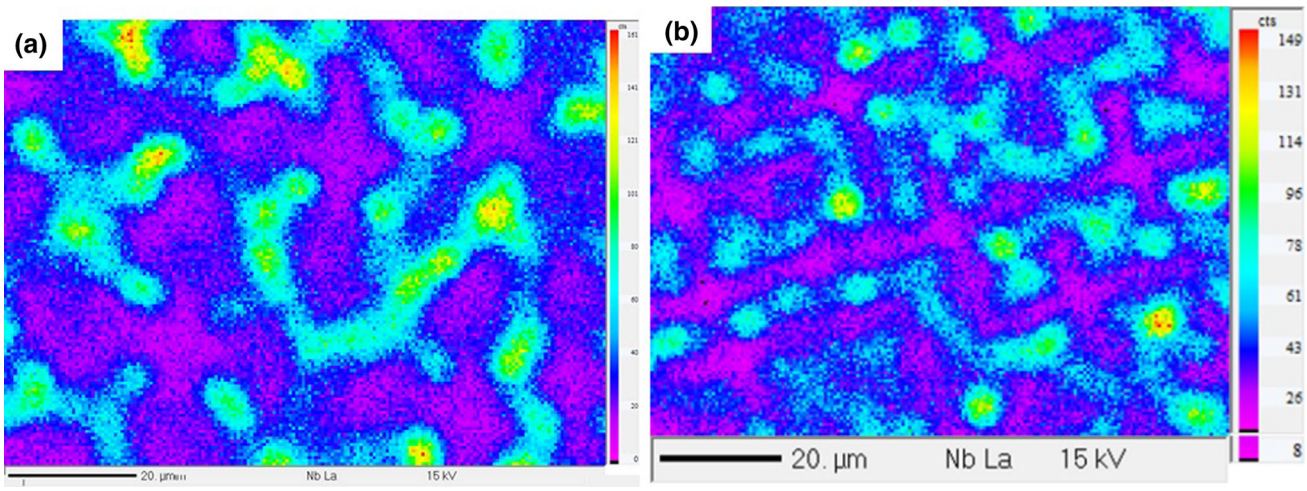

Fig.17—EMPA/WDS elemental mapping showing the concentration of Nb in the (*a*) ASZ and (*b*) DMHAZ.

that they cooled simultaneously under thermodynamic conditions, the calculated result obtained is presented in Figure 18. Although the simulation showed only the precipitation of the γ'' precipitates under equilibrium conditions, the obtained result is in good agreement with the experimental observations. As shown in Figure 18(a), the average size of the strengthening precipitates formed in the interdendritic region of the ASZ (~27 nm) is almost 3 to 4 times that in the interdendritic region of the DMHAZ (~8 nm). This is attributed to the high Nb content in this zone as discussed earlier, and diffusion-induced reduction in Nb content was observed to significantly reduce the precipitation kinetics in the DMHAZ. Similarly in Figure 18(b), the simulated result shows that the volume fraction of the precipitates formed in the ASZ is more than double that of the precipitates formed in the DMHAZ. It is seen that the diffusion of Nb away from the interdendritic regions not only affects the kinetics of the reformed precipitates, but also the extent of their formation. It is thus important to note that, the varying thermal and cooling cycles during WAAM can significantly influence the local composition and sequence of microstructural changes in 718Plus.

3. *Characterization of plate-like particles in deposit*

Plate-like particles were distributed along the interdendritic regions of the deposit, and more of these particles were observed in the bottom than the top region of the deposit. A TEM analysis was carried out on these particles in the as-deposited condition. Although the particles are too small to provide a conclusive analysis, the observed diffraction pattern does not seem to match an orthorhombic crystal structure and not likely to be delta phase particles as reported in the work of Idell *et al.*[19] To increase the size

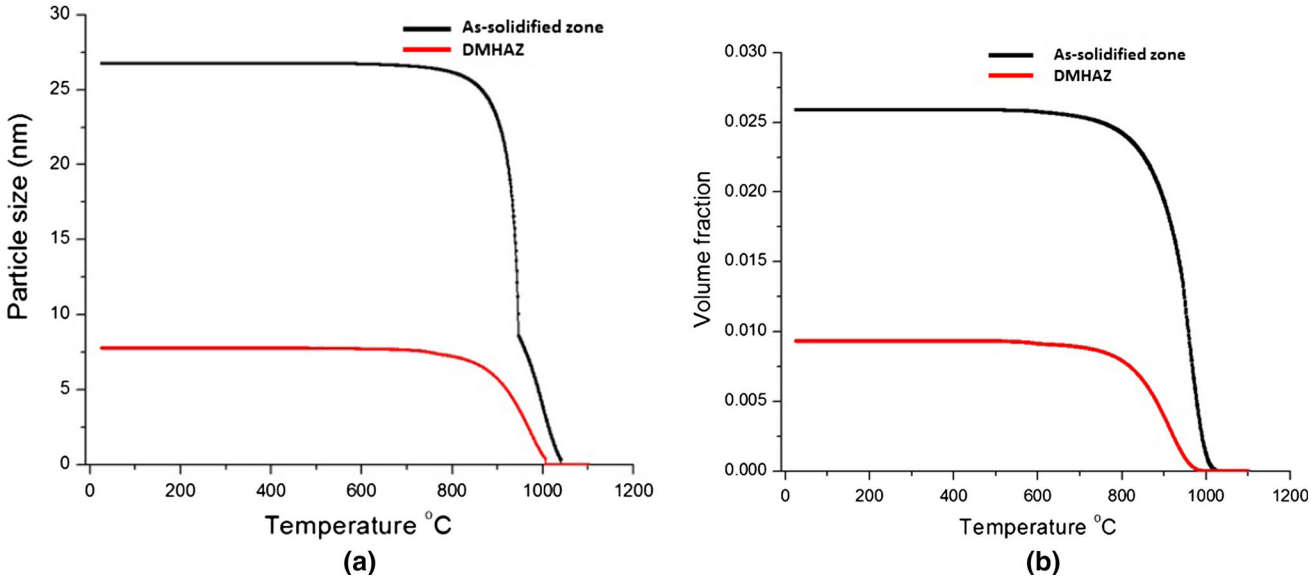

Fig. 18—JMatPro calculation of the strengthening precipitates in the ASZ and the DMAZ showing (*a*) precipitates sizes and (*b*) volume fractions of precipitates.

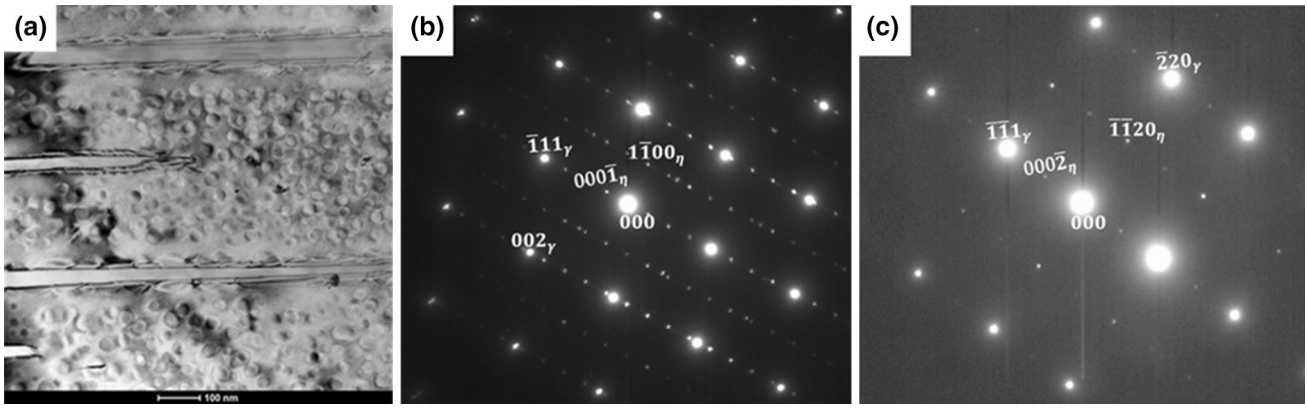

Fig. 19—TEM analysis of the deposit showing (*a*) the BF image of η-phase particles and (*b*) SADP at $[110]_\gamma([11\bar{2}0]_\eta)$ zone axis, and (*c*) SADP $[112]_\gamma([1\bar{1}00]_\eta)$ at zone axis.

of these particles for proper analysis, the deposit was subjected to aging at 1123 K (850 °C) for 48 hours which is believed to be less than the solvus temperature of both the δ and η phases. The SADPs obtained by TEM from the aged deposit by using the zone axes parallel to $[110]_\gamma([11\bar{2}0]_\eta)$ and $[112]_\gamma([1\bar{1}00]_\eta)$ are presented in Figures 19(b) and (c), respectively. The diffraction patterns show that the particles are consistent with the η-ordered hexagonal ($D0_{24}$) structure reported in the grain boundaries of 718Plus by Pickering *et al.*[14] Also, the TEM/EDS mapping and line scan of the particle in Figures 20(a) and (b), respectively, shows the chemical composition of this phase to include Ni, Nb, Al, and some amounts of Ti which is also consistent with the composition of the η Ni_3Ti-like phase reported in 718Plus.[14,15] From the TEM SADP and the TEM/EDS analysis, the plate-like phase formed along the interdendritic region of the deposit is believed to belong to the hexagonal η Ni_3Ti–like phase.

F. *Post-deposition heat-treated microstructure*

Although the presence of strengthening precipitates are seen in the as-deposited condition, as observed from our discussions, they do not form uniformly across the build hence the induced local softness. Therefore, there

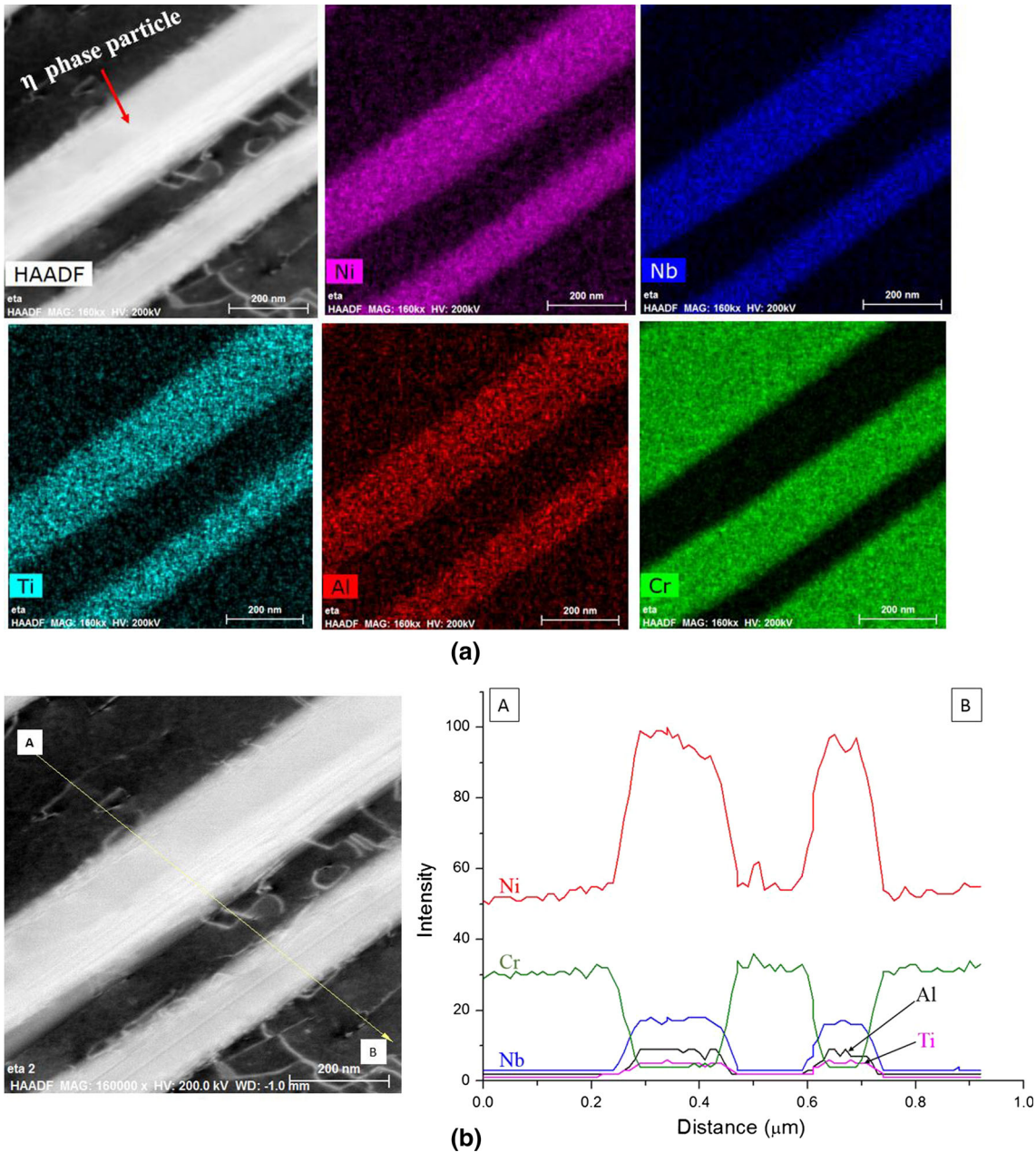

Fig. 20—(*a*) TEM/EDS mapping showing the composition of the η-phase particles and (*b*) TEM/EDS line scan showing the composition profile of the η phase.

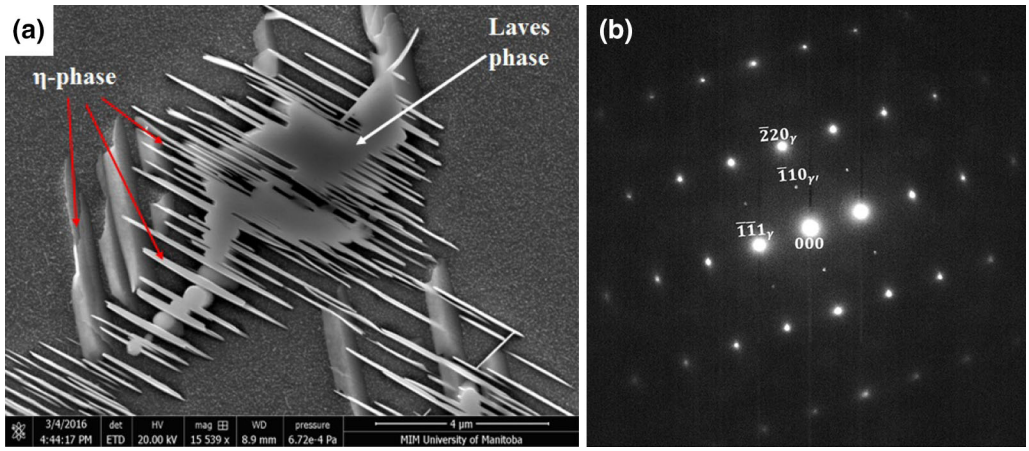

Fig. 21—(*a*) SEM micrograph showing lamellar η-phase particles associated with partially dissolved Laves phase after PDHT and (*b*) TEM SADP showing only γ' reflections after PDHT.

is a need for PDHTs to produce uniform precipitation of the strengthening phase. The deposit was first subjected to a solution heat treatment at 1255 K (982 °C) for 1 hour and then cooled in air. Aging treatment was then carried out at 1061 K (788 °C) for 8 hours, cooling down at about 329 K/h (56 °C/h) to 977 K (704 °C) and holding for another 8 hours before finally cooled in air, as recommended for 718Plus.[46]

The SEM micrograph of the heat-treated deposit is presented in Figure 21(a). It can be seen that there is partial dissolution of the interdendritic Laves phase particles associated with lamellar particles with a plate-like structure that forms simultaneously with the dissolution of the Laves particles. Surprisingly, even with a high content of Nb released from the dissolving Laves phase particles, η-phase particles were found to be linked with the Laves phase in the interdendritic region. It is worth mentioning that these η-phase particles are primarily distributed along the interdendritic region and not the grain boundaries. This may have a significant impact on the mechanical properties of the deposit, especially the intergranular fatigue crack resistance and notch sensitivity, as these properties have been observed to strongly depend on the location and morphology of these precipitates. Therefore, there is the need to further investigate the effect of this microstructure on these mechanical properties of additive manufactured 718Plus. Furthermore, the SEM micrograph also shows uniform precipitation of the strengthening precipitates in the deposit after heat treatment. The spherical morphology of the precipitates suggests that they belong to the γ' phase. TEM analysis was performed to ascertain the nature of the strengthening precipitates, especially to confirm the possible presence of γ'' precipitates in the deposit after the PDHT. The diffraction pattern of the [112] zone axis in Figure 21(b) confirms the presence of only γ' precipitates in the deposit after heat treatment with no superlattice reflections from the γ'' phase observed. It is possible that all of the γ'' precipitates formed during deposition completely dissolved during the solutionizing heat treatment and did not reform during the subsequent aging treatment. This is likely due to the relative homogenization of the segregated elements during the solution heat treatment, thus eliminating local regions with a high Nb content which contributes to the precipitation of γ''. It may thus be inferred that the γ'' phase mainly form in 718Plus when there are local regions with a high content of Nb. Uniform hardness was observed after the recommended treatment throughout the deposit (with hardness values of about 475 HV), and the softening observed in the as-deposited build was no longer found.

IV. CONCLUSIONS

Extensive formation of eutectic solidification micro-constituents including Laves and MC-type carbide phases, induced by micro-segregation, are observed in ATI 718Plus superalloy produced by WAAM process, in the as-deposited condition. In addition, a potentially detrimental softening zone, which has not been previously reported, is found at the DMHAZ of the alloy. Theoretical calculations and experimental observations reveal that the softening is the result of diffusion-induced reduction of Nb content in the interdendritic region of the DMHAZ, which reduces both the extent and the kinetics of the precipitation of the strengthening phase. It is, however, also found that this softening phenomenon can be eliminated by PDHT. Moreover, as revealed by the EBSD analysis, the build has a highly textured microstructure with only few misorientations at the substrate–deposit boundary and the top of the deposit, which is vitally important in the analyses of high temperature mechanical properties of the alloy. Notwithstanding the extensive segregation of Nb in the deposit, the crystallographic structure of the plate-like particles formed in the interdendritic regions is found to be consistent with the $D0_{24}$ η-Ni_3Ti-like phase, in contrast to the δ-phase that is generally reported in IN 718 superalloy. After PDHT, excessive precipitation of the η phase particles is observed to be linked to the partially dissolved Laves phase particles in the interdendritic regions. This type of microstructure is known

to be deleterious to the mechanical properties of 718Plus, and thus may require the design of new heat treatment procedures for 718plus produced by the additive manufacturing process.

ACKNOWLEDGMENTS

Financial support from the Natural Sciences and Engineering Research Council of Canada is gratefully acknowledged.

REFERENCES

1. R. L. Kennedy: in *Superalloys 718, 625, 706 Deriv*., E.A. Loria, ed., TMS, Pittsburgh, PA., 2005, pp. 1–14.
2. M. C. Kushan, C. U. Sinem, Y. Uzunonat, and F. Diltemiz: *Recent Adv. Aircr. Technol*., 2012, pp. 76–96.
3. K. Schreiber, K. Loehnert, and R. F. Singer: in *Proc. Second Symp. Recent Advantages Nb Contain. Mater. Eur. Aerosp. Appl. - A Tech. Commer. Perspect*., Essen, Germany, 2006, pp. 1–5.
4. R.A. Jeniski Jr. and R.L. Kennedy: in *Symp. Recent Advantages Nb-Contain Mater. Eur*., 2006, pp. 1–11.
5. T.D. Bayha, M. Lu, and K.E. Kloske: in *Superalloys 718, 625, 706 Var. Deriv*., E.A. Loria, ed., TMS, Pittsburgh, PA. 2005, pp. 223–32.
6. G. Asala and O.A. Ojo: *Results Phys*., 2016, vol. 6, pp. 196–98.
7. K.R. Vishwakarma, N.L. Richards, and M.C. Chaturvedi: *Mater. Sci. Eng. A*, 2008, vol. 480, pp. 517–28.
8. J. Andersson and G.P. Sjöberg: *Sci. Technol. Weld. Join*., 2012, vol. 17, pp. 49–59.
9. W.D. Cao: in *Superalloys 718, 625, 706 Var. Deriv*., E.A Loria, ed., TMS, Pittsburgh, PA., 2005, pp. 165–77.
10. W.D. Cao and R.L. Kennedy: in *Superalloys*, K.A. Green, T.M Pollock, H. Harada, T.E Howson, R.C Reed, J.J Schirra, and S. Walston, eds., TMS, Seven Springs, PA, 2004, pp. 91–99.
11. R. Kennedy and E. McDevitt: *Adv. Mater. Process*., 2008, vol. 166, pp. 32–33.
12. R.L. Kennedy, W.D. Cao, T.D. Bayha, and R. Jeniski: in *Niobium, High Temp. Appl*., K. Young-Won and C. Tadeu, eds., TMS, San Diego, CA, 2003, pp. 11–21.
13. X. Xie, G. Wang, J. Dong, C. Xu, W.-D. Cao, and R. Kennedy: in *Superalloys 718, 625, 706 Var. Deriv*., E. A. Loria, ed., TMS, Pittsburgh, PA., 2005, pp. 179–91.
14. E.J. Pickering, H. Mathur, A. Bhowmik, O.M.D.M. Messé, J.S. Barnard, M.C. Hardy, R. Krakow, K. Loehnert, H.J. Stone, and C.M.F. Rae: *Acta Mater*., 2012, vol. 60, pp. 2757–69.
15. O.M. Messé, J.S. Barnard, E.J. Pickering, P.A. Midgley, and C.M.F. Rae: *Philos. Mag*., 2014, vol. 94, pp. 1132–52.
16. Eric A Ott, Jon Groh, and Howard Sizek: in *Superalloy 718, 625, 706 Deriv. 2005*, E.A. Loria, ed., TMS, Pittsburgh, PA., 2005, pp. 35–45.
17. M.C. Kushan, S.C. Uzgur, Y. Uzunonat, and F. Diltemiz: *Recent Adv Aircr. Technol*., 2012, vol. 718, pp. 75–96.
18. O. Caballero, G. Sjoberg, and T. Gomez-Acebo: in *7th Int. Symp. Superalloy 718 Deriv*., E. A Ott, J.R Groh, A. Banik, I. Dempster, T.P Gabb, R.Helmink, X. Liu, A. Mitchell, G.P Sjoberg, and Wusatowska-Sarnek, eds., TMS, Pittsburgh, PA., 2010, pp. 689–704.
19. Y. Idell, L.E. Levine, A.J. Allen, F. Zhang, C.E. Campbell, G.B. Olson, J. Gong, D.R. Snyder, and H.Z. Deutchman: *JOM*, 2016, vol. 68, pp. 950–59.
20. Y. Idell, C. Campbell, L. Levine, F. Zhang, G. Olson, and D. Snyder: *Microstruct. Microanal*., 2015, vol. 21, pp. 465–66.
21. R.G. Ding, Z.W. Huang, H.Y. Li, I. Mitchell, G. Baxter, and P. Bowen: *Mater. Charact*., 2015, vol. 106, pp. 324–37.
22. Y. Long, P. Nie, Z. Li, J. Huang, X. Li, and X. Xu: *Trans. Nonferrous Met. Soc. China*, 2016, vol. 26, pp. 431–36.
23. G. Asala, J. Andersson, and O.A. Ojo: *Int. J. Adv. Manuf. Technol*., 2016, vol. 87 (9), pp. 2721–29.
24. D. Ding, Z. Pan, D. Cuiuri, and H. Li: *Int. J. Adv. Manuf. Technol*., 2015, vol. 81, pp. 465–81.
25. S.W. Williams, F. Martina, A.C. Addison, J. Ding, G. Pardal, and P. Colegrove: *Mater. Sci. Technol*., 2015, vol. 32, pp. 641–47.
26. Yuan. Tian, Donald. McAllister, Hendrik. Colijn, Michael. Mills, Dave. Farson, Mark. Nordin, and Sudarsanam. Babu: *Metall. Mater. Trans. A*, 2014, vol. 45A, pp. 4470–83.
27. William.J. Sames, Kinga.A. Unocic, Ryan.R. Dehoff, Tapasvi. Lolla, and Sudarsanam.S. Babu: *J. Mater. Res*., 2014, vol. 29, pp. 1920–30.
28. E. Biro, S. Vignier, C. Kaczynski, J.R. McDermid, E. Lucas, J.D. Embury, and Y.N. Zhou: *ISIJ Int*., 2013, vol. 53, pp. 110–18.
29. N.T. Yamauchi, T. Taka, K. Kunishige, and N. Nagao: *Trans. Iron Steel Inst. Jpn*., 1982, vol. 22, p. B107.
30. A. Segerstark, J. Andersson, and L.-E. Svensson: *Sci. Technol. Weld. Join*., 2017, vol. 1, pp. 1–9.
31. O.A. Idowu, O.A. Ojo, and M.C. Chaturvedi: *Weld. J*., 2009, vol. 88, pp. 179–87.
32. D. Clark, M.R. Bache, and M.T. Whittaker: *J. Mater. Process. Technol*., 2008, vol. 203, pp. 439–48.
33. X. Xie, J. Dong, G. Wang, W. You, J. Du, C. Zhao, Z. Wang, and T. Carneiro: in *Proc. Int. Symp. Superalloys Var. Deriv*., E. A. Loria, ed., TMS, Pittsburgh, PA., 2005, pp. 287–98.
34. R. Cozar and A. Pineau: *Metall. Trans*., 1973, vol. 4, pp. 47–59.
35. H.L. Eisellstein: *Adv. Technol. Stainl. Steels*., 1965, vol. 369, pp. 62–75.
36. M. Sundararaman, P. Mukhopadhyay, and S. Banerjee: *Metall. Trans. A*, 1992, vol. 23, pp. 2015–28.
37. T. Alam, M.C. Chaturvedi, S.P. Ringer, and J.M. Cairney: *Mater. Sci. Eng. A*, 2010, vol. 527, pp. 7770–74.
38. S. Nalawade, M. Sundararaman, J.B. Singh, A. Verma, and R. Kishore: *Trans. Indian Inst. Met*., 2010, vol. 63, pp. 35–41.
39. Y. Chen, F. Lu, K. Zhang, P. Nie, S.R.E. Hosseini, K. Feng, and Z. Li: *J. Alloys Compd*., 2016, vol. 670, pp. 312–21.
40. Y. Chen, K. Zhang, J. Huang, R.S.E. Hosseini, and Z. Li: *Mater. Des. J*., 2016, vol. 90, pp. 586–94.
41. R. Thamburaj and J.A. Goldak: *Int. Met. Rev*., 1983, vol. 28, pp. 2–21.
42. G.P. Dinda, A.K. Dasgupta, and J. Mazumder: *Scr. Mater*., 2012, vol. 67, pp. 503–06.
43. K.T. Makiewicz: *Master's Thesis*, The Ohio State University, Columbus, OH, 2013.
44. X.L. Pan, H.Y. Yu, G.F. Tu, W.R. Sun, and Z.Q. Hu: *Trans. Nonferrous Met. Soc. China*, 2011, vol. 21, pp. 2402–07.
45. R.V. Patil and G.B. Kale: *J. Nucl. Mater*., 1996, vol. 230, pp. 57–60.
46. W.D. Cao and R.L. Kennedy: *Recommendations for Heat Treating Allvac 718Plus*® Alloy Parts, Monroe, NC, 2006.